Water Resources Research

RESEARCH ARTICLE
10.1029/2018WR023250

# High-Resolution Global Water Temperature Modeling

**Niko Wanders**[1,2], **Michelle T. H. van Vliet**[3], **Yoshihide Wada**[1,4], **Marc F. P. Bierkens**[1,5], **and Ludovicus P. H. (Rens) van Beek**[1]

[1]Department of Physical Geography, Utrecht University, Utrecht, The Netherlands, [2]Department of Civil and Environmental Engineering, Princeton University, Princeton, NJ, USA, [3]Water Systems and Global Change Group, Wageningen University, Wageningen, The Netherlands, [4]International Institute for Applied Systems Analysis, Laxenburg, Austria, [5]Deltares, Utrecht, The Netherlands

**Key Points:**
- Development of a simulated high-resolution global water temperature data set and high-resolution physically based model is presented
- Increased spatial resolution results in a better performance against global in situ observations
- An average increase of 0.16 degrees Celsius per decade is found for global water temperature between 1960 and 2014

**Correspondence to:**
N. Wanders,
n.wanders@uu.nl

**Citation:**
Wanders, N., van Vliet, M. T. H., Wada, Y., Bierkens, M. F. P., & van Beek, L. P. H. (Rens) (2019). High-resolution global water temperature modeling. *Water Resources Research*, *55*, 2760–2778. https://doi.org/10.1029/2018WR023250

Received 3 MAY 2018
Accepted 4 MAR 2019
Accepted article online 12 MAR 2019
Published online 5 APR 2019



**Abstract** The temperature of river water plays a crucial role in many physical, chemical, and aquatic ecological processes. Despite the importance of having detailed information on this environmental variable at locally relevant scales (≤50 km), high-resolution simulations of water temperature on a large scale are currently lacking. We have developed the dynamical 1-D water energy routing model (DynWat), that solves both the energy and water balance, to simulate river temperatures for the period 1960–2014 at a nominal 10-km and 50-km resolution. The DynWat model accounts for surface water abstraction, reservoirs, riverine flooding, and formation of ice, enabling a realistic representation of the water temperature. We present a novel 10-km water temperature data set at the global scale for all major rivers, lakes, and reservoirs. Validated results against 358 stations worldwide indicate a decrease in the simulated root-mean-square error (0.2 °C) and bias (0.7 °C), going from 50- to 10-km simulations. We find an average global increase in water temperature of 0.16 °C per decade between 1960 and 2014, with more rapid warming toward 2014. Results show increasing trends for the annual daily maxima in the Northern Hemisphere (0.62 °C per decade) and the annual daily minima in the Southern Hemisphere (0.45 °C per decade) for 1960–2014. The high-resolution modeling framework not only improves the model performance, it also positively impacts the relevance of the simulations for regional-scale studies and impact assessments in a region without observations. The resulting global water temperature data set could help to improve the accuracy of decision-support systems that depend on water temperature estimates.

## 1. Introduction

The temperature of river water plays a crucial role in many physical, chemical, and biological processes (van Vliet, Yearsley, Franssen, et al., 2012). Changes in water temperature affect the solubility of gases, the metabolic rate of aquatic flora and fauna, the rate of open water evaporation, and the formation of ice. Moreover, the influence of changing water temperatures is not only felt locally but also has regional and downstream impacts (Olden & Naiman, 2010). Increases in water temperature can reduce the cooling potential of a volume of water for energy production (van Vliet, van Beek, et al., 2016), increasing the water demand of thermoelectric power plants to keep up with the energy demand. The decreased solubility of dissolved oxygen with increasing water temperatures (Ozaki et al., 2003), leads to reduced oxygen availability for aquatic fauna and potential fish kill (e.g., Matthews & Berg, 1997; Lessard & Hayes, 2003) or favorable conditions for Cyanobacteria (Robarts & Zohary, 1987). Increased open water evaporation due to higher temperatures in large water bodies will reduce the water availability for hydropower and irrigation (Wanders & Wada, 2015a) while consequently also reducing the industrial cooling potential of the remaining water. The formation of ice can impede flow in river systems and lead to flooding upstream. This creates a need for detailed spatial temporal information on the distribution of water temperatures globally in space and time. This is even more relevant in regions that lack observations and where modeling provides the only solution to acquire long-term water temperature estimates.

Even though we have large amounts of observations for water quantity (discharge) collected in the Global Runoff Data Centre (GRDC), observations of water temperature in rivers, lakes, and reservoirs (hereafter, water temperature) are very sparse. Most of these observations are concentrated in the continental USA, Europe, and southeast Asia (Figure 1) and are located in major river basins. Therefore, we have relatively little knowledge of the state of water temperature for many smaller- and medium-sized rivers, in particular

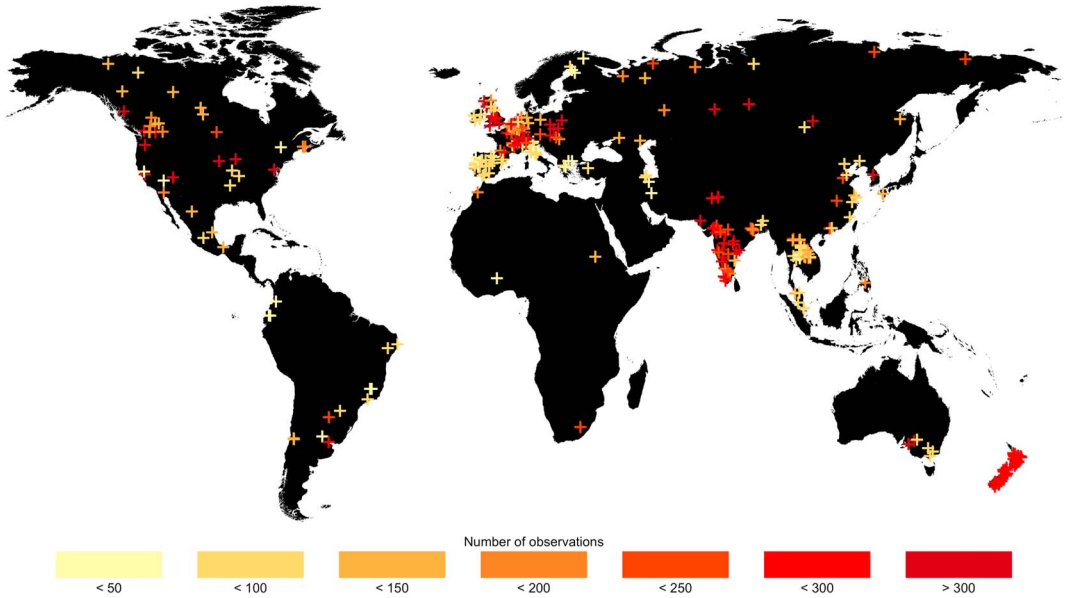


**Figure 1.** Validation locations.

for South America and Africa. By deploying models, many local and regional studies have tried to provide estimates of the water temperature in these ungauged regions or for confined water bodies.

Modeling efforts can be generally divided into two groups, statistical and physically based approaches (Caissie, 2006). Statistical approaches estimate the water temperature by using a regression, stochastic relation, or machine learning technique to estimate water temperature as a function of air temperature, discharge and other variable (Morrill et al., 2005; Moore, 2006; Smith, 1981). These methods often lead to satisfactory results; however, these statistical relationships need to be determined based on available observations. In addition, statistical methods are prone to unrealistic simulations under changing conditions in the case of extrapolation (e.g., projections of future water temperature; Morrill et al., 2005). Statistical models have been widely deployed in modeling water temperature at country and basin level (e.g., DeWeber & Wagner, 2014); however, global applications are sparse (e.g., Punzet et al., 2012; van Vliet et al., 2011).

Physically based models, on the other hand, use physical relations between water temperature and meteorological and hydrological variables to estimate the exchange of energy between the river and the atmosphere (e.g., Caissie et al., 2007; Edinger et al., 1968; St-Hilaire et al., 2000). Limitations of physically based models are that they have large data requirements and larger computational requirements compared to statistical methods (e.g., Caissie, 2006). Physically based water temperature models have been used to simulate water temperature in individual lakes (e.g., Bueche & Vetter, 2014), major river basins (e.g., Pike et al., 2013; van Vliet, Yearsley, Franssen, et al., 2012), and for coarse-resolution global simulations of historic (e.g., van Beek et al., 2012) and future projections of water temperature (e.g., Punzet et al., 2012; van Vliet et al., 2013; van Vliet, van Beek, et al., 2016). Their advantage over statistical methods is most predominant in ungauged basins or assessing the impact of climate change on the water temperature. Physical-based water temperature models allow for water temperature estimates in unobserved conditions since they follow physical relationships to derive water temperature estimates from climatic and hydrological input data. The quality of these estimates will, however, be dependent on the model's ability to accurately represent these physical relationships, which can be evaluated with observation in other regions. Physical models simulate the transport of energy along the river network and changes therein, whereas this is impossible for existing statistical water temperature models to achieve. That makes physically based water temperature models highly suited to apply at the global scale in ungauged basins and in the context of a changing climate.

We have global simulations at a coarser gridded 50-km spatial resolution or even coarse; however, at these coarse resolutions we are not capable of simulating all the relevant processes (e.g., van Beek et al., 2012). Thus, we lack consistent high-resolution water temperature estimates at spatial scales relevant to water managers of small- and medium-sized river basins ($\leq$50 km). Here we present a novel stand-alone 1-D dynamic

energy routing model (DynWat) that solves both the energy and mass balance of the river system simultaneously and provides water temperature estimates at 10-km spatial resolution. The model takes into account the mixing in lakes and reservoir operations that alter the water availability in downstream regions. In addition, it simulates floodplain inundation and ice formation to allow for more realistic simulations of water quantity and temperature.

The objectives of this study are (1) develop a new physically based water temperature model, (2) provide a high-resolution global water temperature data set to be used in other studies, (3) evaluate the performance of the water temperature data set and trends in water temperature for the period 1960–2014.

The model equations and assumption are introduced in section 2, followed by an evaluation of the model performance (section 3.1), the results at the global scale (sections 3.2 and 3.3), and finally a discussion and conclusion on the potential applications and impact of these new simulations (section 4).

## 2. Materials and Methods

### 2.1. DynWat Model

In this study we used a Dynamic Water temperature model (DynWat) that solves the transport of water and energy in the river network. The model has been significantly adapted from van Beek et al. (2012), which includes processes such as the lateral transport of energy, ice formation, and ice breakup. We included additional processes to cover the breakup of ice, thermal mixing in large water bodies, including a dynamic coupling for surface water abstraction and reservoirs operations, and allow for finer spatial resolution simulations by improving model stability at these high resolutions. The original model already included the lateral transport of energy, ice formation, and ice breakup, but the updated model is able to simulate daily water temperatures with 5 min (or finer) temporal disaggregation to ensure stable model simulations in smaller streams and lakes. Finally, the new model can be used in a stand-alone configuration to allow off-line coupling with other hydrological models; for this the model needs hydrological inputs on the following:

1. direct runoff or surface runoff;
2. interflow;
3. baseflow or groundwater discharge; and
4. simulated or estimated temperature of these fluxes

from any land surface model. In the stand-alone configuration the model will also need additional information on the meteorological input, such as temperature, precipitation, and radiation terms. There is a possibility to include the internal land surface water temperature of direct runoff, interflow, and baseflow generated by the hydrological model directly in the DynWat model.

#### 2.1.1. Energy Balance

We assume that each channel has a rectangular shape and full vertical mixing. Within each fully mixed water volume we solve the surface water energy balance, following van Beek et al. (2012):

$$\rho_w C_p \frac{\partial(hT_w)}{\partial t} = \rho_w C_p \frac{\partial(vhT_w)}{\partial x} + S_{in}(1-\alpha_w) + L_{\text{in}} - L_{\text{out}} - H - LE + \rho_w C_p \int_{x=0}^{dx} q_s T_s \tag{1}$$

where $T_w$ is the water temperature (°K). The parameter $\rho_w$ is the density of water (1,000 kg/m$^3$), $C_p$ is the heat capacity of water (4,190 J·kg$^{-1}$· K$^{-1}$), $h$ is the water height (m), $v$ is the velocity of water derived from solving the kinematic wave equation (m/s). $S_{\text{in}}$ is the incoming shortwave radiation (J·s$^{-1}$·m$^{-2}$) that is reflected with $(1 - \alpha_w)$, where $\alpha_w = 0.15$ for open water. $L_{\text{in}}$ is the incoming longwave radiation (J·s$^{-1}$·m$^{-2}$), and the outgoing radiation ($L_{\text{out}}$) is calculated by the Boltzmann's equation given by

$$L_{\text{out}} = \varepsilon \sigma T_w^4 \tag{2}$$

where $\varepsilon$ is the emissivity (taken as 1 for this study) and $\sigma$ is the Boltzmann constant (J°/K). The sensible heatflux ($H$, J·s$^{-1}$·m$^{-2}$) is calculated using the difference between water and air temperature and given by

$$H = k_H(T_w - T_{\text{air}}) \tag{3}$$

where $k_H$ is the turbulent heat exchange coefficient (20 J·s$^{-1}$·m$^{-2}$·K$^{-1}$). The latent heat ($LE$, J·s$^{-1}$·m$^{-2}$) is given by

$$LE = \lambda_w \rho_w ET \tag{4}$$

where $\lambda_w$ is the latent heat of water vaporization (250 kJ·kg$^{-1}$·K$^{-1}$) and ET is the actual evaporation (m/s). Potential evapotranspiration is calculated using the Penman evapotranspiration formulation, using temperature, radiation, and wind. Taking into account the nature of the water body (deep or shallow water, ice cover, etc), water is evaporated at the potential rate as long as the quantity is sufficient. It should be noted that only three driving fluxes are taken from PCR-GLOBWB (or any other land surface model) to drive the model (surface runoff, interflow, and baseflow); all meteorological forcing is directly imposed. The lateral fluxes $q_s$ (m/s) into the river channel are given by

$$q_s = q_{\mathrm{dr}} + q_i + q_b \tag{5}$$

where, $q_{\mathrm{dr}}, q_i, and\ q_b$ are the direct runoff, interflow/stormflow, and baseflow, respectively. The land surface model specifies the runoff from the land surface that reach the river network and that are subsequently used in DynWat. Direct runoff result from infiltration excess or saturation excess overland flow (from rainfall or snowmelt). Interflow/stormflow arises from lateral flow in soils on the boundary of soil and bedrock. Base flow is the outflow from the groundwater reservoir which is linearly proportional to the storage. The average temperature of these runoff components ($T_s$) is provided by

$$T_s = \frac{q_{\mathrm{dr}}}{q_s} \max(T_{\mathrm{ice}}, T_{\mathrm{air}} - 1.5) + \frac{q_i}{q_s} \max(T_{\mathrm{ice}}, T_{\mathrm{air}}) + \frac{q_b}{q_s} \max(T_{\mathrm{ice}} + 5.0, \overline{T_{\mathrm{air}}}) \tag{6}$$

where the direct runoff has a temperature 1.5 °C lower than the air temperature, interflow has a temperature equal to the air temperature and the baseflow temperature is equal to the annual average air temperature (derived from the meteorological input). Rain temperature, and hence direct runoff temperature, is reduced by 1.5 °C from the air temperature to account for the cooling of rain during the free-falling phase (Byers et al., 1949). A minimum temperature of 5 °C is assumed for the baseflow to ensure that the water does not freeze upon entering the channel network. Locations with annual average temperatures lower than this threshold are likely heavily influenced by permafrost and will have a limited baseflow component. Using the hydrological input from the land surface model PCR-GLOBWB 2 (Sutanudjaja et al., 2018) in the study, temperature estimates of the different terrestrial hydrological fluxes (direct runoff, interflow, and baseflow) have to be made. If the land surface model coupled to DynWat has an internal energy balance included, $T_s$ can be derived from the internal energy budget of the land surface.

#### 2.1.2. Ice Cover

When the water temperature reaches 0 °C, ice growth will occur in the model. We assume that under the ice we have a fully mixed water volume with an ice layer on top. In contrast to van Beek et al. (2012), we do simulate mechanical ice breakup, by imposing a minimum ice thickness of 5 mm in flowing water in the melting period. The broken ice and its energy are then laterally transported along the river channel, to ensure full closure of the energy balance and mimic realistic ice transportation processes. If the ice thickness exceeds the 5 mm due to refreezing, the mobility of the ice is reduced. The channel roughness is no longer affected when the ice is freely flowing. Changes in the ice thickness because of expansion or decreasing water surface area are accounted for by the model do allow ice formation in floodplain areas. Under all frozen conditions the new surface water and ice energy balance are given by

$$\begin{aligned} \rho_w C_p \frac{\partial (hT_w)}{\partial t} = \rho_w C_p \frac{\partial (vhT_w)}{\partial x} + S_{\mathrm{in}}(1 - \alpha_{\mathrm{ice}}) + L_{\mathrm{in}} - L_{\mathrm{out}} - H \\ + \rho_w C_p \int_{x=0}^{\mathrm{dx}} q_s T_s \end{aligned} \tag{7}$$

the ice layer on the water surface reduces the incoming shortwave by increasing the reflection, given by $\alpha_{\mathrm{ice}} = 0.8$ for ice cover with a snow layer. $LE$ is eliminated since we do not account for sublimation and no evaporation occurs from the frozen water surface. $H$ is calculated using the difference between ice and air temperature:

$$H_{\mathrm{ice}\rightarrow\mathrm{air}} = k_H(273.15 - T_{\mathrm{air}}) \tag{8}$$

where 273.15 °K is the ice temperature. The energy balance and the thickness of the ice sheet can be calculated by

$$\lambda_f \rho_w \frac{\partial z}{\partial t} = -H_{w\rightarrow \text{ice}} + H_{\text{ice}\rightarrow \text{air}} - S_{\text{in}}(1-\alpha_{\text{ice}}) - L_{\text{in}} + L_{\text{out}} \tag{9}$$

where $\lambda_f$ is the heat of fusion of ice (333.4 kJ/kg) and $z$ is the ice thickness (m). The sensible heat from the water to the ice is given by

$$H_{w\rightarrow \text{ice}} = k_{\text{wi}}(T_w - 273.15) \tag{10}$$

where $k_{\text{wi}}$ is the heat exchange coefficient between water and ice (8 $\text{J}\cdot\text{s}^{-1}\cdot\text{m}^{-2}\cdot\text{K}^{-1}$).

#### 2.1.3. Floodplain

The simulation of floodplains is important as the surface area increases with the water volume, leading to inundation. This increased surface area increases the energy exchange between the water volume and the atmosphere, thus allowing for faster heating or cooling of the water volume. Floodplain water storage can also act as an energy buffer that causes regulation of the incoming lateral energy fluctuations and therefore reduces fluctuations in downstream water temperatures. In DynWat we assume that the water in the channel and that on the floodplain are fully mixed, which will have a slight impact on the energy buffering capacity of the floodplain. Inundation also increases the resistance experienced by the flow, especially along the more densely vegetated floodplains, and results in a slower flood wave propagation. To simulate floodplain effects, subgrid elevation profiles are used to distribute the channel storage in excess of the channel depth within the grid cell. The volume is therefore related to the total flooded area and allows the model to compute the total fraction of flood area. This approach is adopted from the current floodplain implementation in PCR-GLOBWB 2 (Sutanudjaja et al., 2018) and allows for more accurate simulation of the discharge and water temperature.

#### 2.1.4. Channel Roughness

In general, the channel roughness coefficient is a function of the water volume and the channel wetted perimeter. In DynWat there are two additional factors that impact the surface roughness, flood plains and ice cover. In general, the roughness of the channel is used to compute the stage-discharge relation of the channel. The flow velocity is dependent on the channel roughness, where a higher roughness will cause lower flow velocities and consequently stronger flood wave damping. A detailed description on the kinematic wave routing procedure used in DynWat can be found in Winsemius et al. (2013) and Sutanudjaja et al. (2018).

The Manning's roughness coefficient under nonflood and ice-free conditions ($n_c$, $\text{s/m}^{1/3}$) equals 0.04 following Sutanudjaja et al. (2018), which equals clean and winding streams. When the channel storage exceeds the potential channel storage, water flows into the floodplains which have a higher roughness due to the presence of tall vegetation that is not permanently flooded. Following Winsemius et al. (2013) the equation is modified to

$$n = \sqrt[1.5]{\frac{P_c}{P_c+P_f} n_c^{1.5} + \frac{P_f}{P_c+P_f} n_f^{1.5}} \tag{11}$$

where $n_f$ is the Manning's coefficient of the floodplain (−), and $P_c$ and $P_f$ are the wetted perimeters of the channel and floodplain, respectively. For the floodplains $n_f$ is constant and set to 0.1 to represent floodways with heavy stand of timber and underbrush. In case of ice cover, the $P_r$ increases due to the ice cover that adds friction on the top of the channel. This changes the equation to

$$n = \sqrt[1.5]{\frac{P_c}{P_c+w} n_c^{1.5} + \frac{w}{P_c+w} n_i^{1.5}} \tag{12}$$

where $w$ is the river width and $n_i$ is the Manning's coefficient of ice. We use the empirical relationships derived by Nezhikovskiy (1964) and given by

$$n_i = 0.0493 h^{-0.23} z^{0.57} \tag{13}$$

where $h$ is the water depth (m) and $z$ is the ice thickness (m).

#### 2.1.5. Lakes and Reservoirs

The equations above hold true for fully vertically mixed water volumes, which is not the case for lakes and reservoirs where the surface water energy balance is solved only for the well-mixed epilimnion and the underlying thin metalimnion (thermocline) that are thermally active. For lakes and reservoirs, the depth of the thermocline ($D_t$) is derived from Davies-Colley (1988) and calculated by

$$D_t = 9.52 f^{0.425} \tag{14}$$

where $f$ is the fetch length of a water body. The fetch length is obtained from the GRanD database (Lehner et al., 2011), where we assume a rectangular shape for natural water bodies and a triangular shape is used for a reservoir (Liebe et al., 2005). This representation of waterbodies creates a faster thermal response in deep waterbodies that would otherwise have a significant cooling effect on the downstream water temperature. If a thermocline develops the energy and water below the thermocline remains inactive as long as the thermocline persists. In that case, only water and energy are exchanged with the water volume above it. When the temperature profile becomes unstable (e.g., in spring or autumn), the profile is inverted and full mixing of the total water volume and the associated energy occurs. We presently exclude human influences such as the release of cooling water and cold water releases from reservoirs in DynWat. A lack of detailed global observations does not allow the model to constrain these operations in a realistic fashion. Reservoir operations in the current version of the model are optimized for hydropower, and similar to the reservoir operations currently implemented in PCR-GLOBWB 2 (Sutanudjaja et al., 2018). In general the reservoir storage is kept between 30% and 70% of the full capacity and the outflow is scaled proportionally to the annual average discharge. When the storage exceeds 70% the outflow is increased up to bankfull discharge to prevent reservoir flooding while avoiding downstream flooding. Similarly, reservoir outflow is reduced to prevent complete exhaustion of reservoir storage if a drought were to occur.

### 2.2. Comparing Model Resolutions

To evaluate the performance of the high-resolution DynWat model, we use water temperature simulations at two spatial resolutions of roughly 10 and 50 km at the equator (Table A1). Note that the 50-km resolution is that of previous studies on global water temperature modeling (van Vliet, Yearsley, Ludwig, et al., 2012; van Beek et al., 2012) The model solves the surface water energy balance at the daily timestep, with temporal disaggregation of a 5-min subtimestep for numerical stability.

In each timestep, the model uses daily runoff estimates from the global hydrological model PCR-GLOBWB (Sutanudjaja et al., 2018) as input to the routing model. The input is separated into direct runoff ($q_{\mathrm{dr}}$), interflow ($q_i$), and baseflow ($q_b$) to allow for computation of the runoff temperature ($T_s$, equation (6)). Both DynWat and PCR-GLOBWB 2 use ERA-40 and ERA-Interim forcing (Berrisford et al., 2011; Dee et al., 2011; Uppala et al., 2005), with an elevation correction to account for spatial heterogeneity in the elevation (Sutanudjaja et al., 2018), to generate water temperature and runoff estimates for the period 1960–2014. The hydrological input from PCR-GLOBWB 2 has been extensively validated in multiple studies and shown to produce accurate estimates of daily discharge (Sutanudjaja et al., 2018; Van Beek et al., 2011), simulate hydrological extreme events (e.g., He et al., 2017; Marx et al., 2018; Thober et al., 2017; Wada et al., 2013; Wanders & Van Lanen, 2015), and reproduce decadal teleconnections (e.g., Wanders & Wada, 2015b). The river routing in DynWat is similar to that of PCR-GLOBWB and for the discharge simulation performance, we refer to Sutanudjaja et al. (2018) for the latest evaluation.

In addition to these two physically based scenarios, we used air temperature. As a comparable "simulation" we use air temperature as a proxy for the water temperature (Table A1), which is often done when a water temperature model is not available. This is not an advanced statistical method as used for more complete statistical water temperature models; however, it will serve as a "poor man's" approximation for water temperature and to provide some indication of the skill of the physically based simulations. Here we use weekly average air temperature to have an estimate of the water temperature at that particular location as a predictor of the water temperature. While ideally one would like to deploy a temporal averaging of the air temperature based on the water bodies or river size, or calibration of the aggregation period at the global scale (e.g., Punzet et al., 2012), this is beyond the aims of this study. Therefore, we have adopted a constant weekly aggregation to simulate medium sized. We will show the impact on the air temperature model performance for the different stream sizes, to provide some insight into the impact of this decision.

This temperature-based method does not include any buffering effects that occur in lakes but acts as a good proxy for water temperature when no physically based or statistical model is available.

### 2.3. Evaluation Metrics

The different scenarios are compared to observations from the United Nations Environment Programme Global Environment Monitoring System (GEMS) data set at a total of 358 locations (Figure 1). Most locations are located in the Northern Hemisphere, with a bias toward Europe, the United States, and southeast Asia. We have an average of 300 observations for each station, where some stations have daily observations, and some have sparse instantaneous measurements on a 4-weekly level. We evaluate the scenario performance based on the correlation coefficient (R) and root-mean-square error (RMSE) between daily observations and simulations.

### 2.4. Spatial Trend Analysis

To study the effect of changes in the historic climate, we compute the trends in the water temperature simulations. We use a linear trend estimate to find the degree of change in the water temperature over the period 1960–2014. We only assume linear trends when testing for a significant deviation from the no change baseline with a $p < 0.05$. We exclude rivers with discharge <10 $m^3/s$ for the spatial trend analysis, because smaller rivers are likely not to have enough heat-carrying capacity and their trends in $T_w$ are likely only to show trends in local $T_{air}$. The linear trend analysis is performed for the annual mean, minimum, and maximum $T_w$. In addition, we will perform a comparison between the trends in annual mean $T_w$ and $T_{air}$ to evaluate the impact of lateral energy transport on local trends in $T_w$. This comparison will also show where it is important to use one of the physically based $T_w$ simulations compared to the benchmark $T_{air}$ model run.

## 3. Results

### 3.1. Validation of Modeled Water Temperatures

In general, we observe a performance improvement with increasing spatial resolution of the model simulations (Figure 2). We can distinguish a clear benefit in the correlation values when using DynWat over the benchmark approximation that $T_w$ = weekly average $T_{air}$. The advantage of the higher resolution is less evident as no significant difference was found for the 50-km (median daily $R = 0.869$) resolution compared to the 10 km (daily $R = 0.861$). We do observe a significant improvement (90% confidence level) for the median RMSE values, from 3.4 °C (50 km) to 3.2 °C (10 km) with the $T_{air}$ scenario showing a RMSE of 4.0 °C. In the median RMSE, we observe a decrease of 0.2 °C for individual locations for all the catchment sizes. This indicates that the higher-resolution model shows lower deviations from the observed temperature and is better able to simulate the observed water temperatures. The highest impact is found for rivers with a discharge <10 $m^3/s$, where the input of the land surface model PCR-GLOBWB 2 has shown to provide more reliable runoff simulations at the finer 0.0833° resolution (Sutanudjaja et al., 2018). The water temperature model benefits from these improved runoff estimates, resulting in a reduction in RMSE.

Figure 2 shows that none of the observed rivers have an RMSE close to 0 °C, which could be explained by the spatial mismatches in station locations and model simulations. The model simulations provide the channel (or lake) average water temperature, whereas the observations are taken at specific water depths. For most systems we can assume a fully mixed system; however, some rivers will have temperature gradients within the water profile.

In general we observe that model biases reduce with increasing spatial resolution of physical realism of the simulations (Figure 2). The 10-km simulations have an average bias of only −0.3 °C, which is significantly lower than the −1.0 °C and −2.1 °C found for the 50 km and $T_{air}$, respectively. The improvement in the bias is equally distributed across the different catchment sizes indicating a global improvement in the water temperature bias going from 50 km to the finer 10-km resolution.

Difference between the two physically based applications at different spatial resolutions (10 and 50 km) can be attributed to the statistical elevation correction of the temperature, finer spatial resolution of the land surface parameterization, and changes in the hydrodynamic network. The increased physical realism in the simulations resulted in improvements in the $R$ (median improvement = 0.01), RMSE (0.1 °C) and model bias (0.23 °C, Figure A1). Maps of the performance metrics can be found in the appendix in Figure A2.

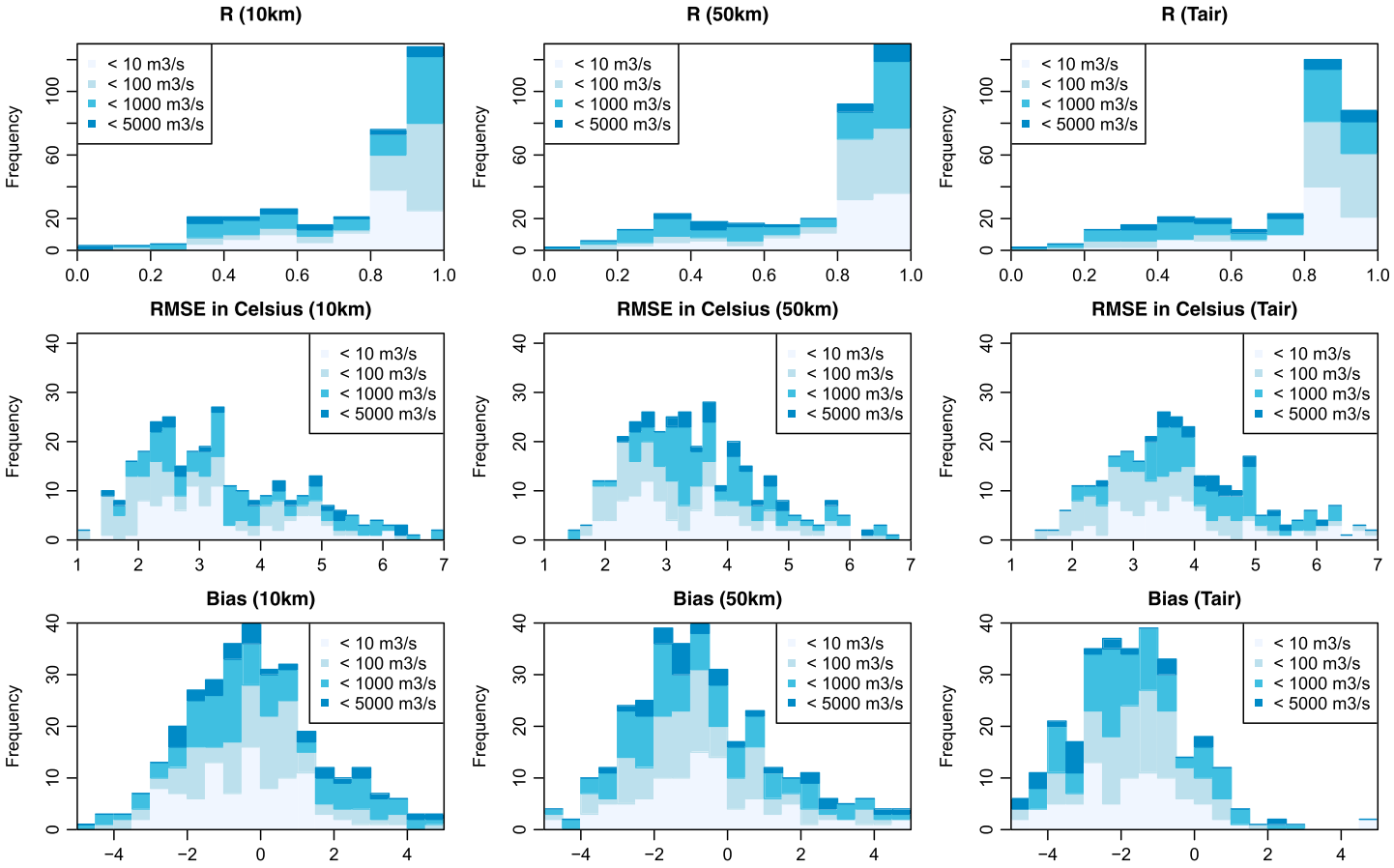


**Figure 2.** Evaluation of global water temperature simulations: Top row gives the correlation (R) between simulated and observed for different river sizes. Middle row gives the root-mean-square error (RMSE) for the three simulation scenarios. Bottom row gives the bias between observed and simulated water temperatures for the three simulation scenarios.

Detailed time series of individual rivers show that the simulated water temperature shows similar behavior to the observed time series. They also show that the coarse-resolution simulation shows a more rapid response to changes in air temperature and radiation (Figure 3). The coarse $T_w$ simulations show a higher degree of variability indicating a closer resemblance to the more rapid changes in the air temperature signal. This is likely caused by the lower channel and groundwater storage capacity in the coarse scale simulations, which is a result of the upscaling of the groundwater parameterization in the hydrological model and upscaling of the precipitation input (Table A1). The coarser groundwater parameterization results in an on-average faster groundwater response to precipitation, as the very slow responding groundwater aquifers are spatially aggregated with faster responding regions. In addition, we observe that the spatial heterogeneity in channel roughness results in longer travel times of the river discharge in the 10-km simulations. We have also observed a shortened lagged cross correlation between anomalies in $T_{\text{air}}$ and $T_w$ for the 50-km simulation, confirming this hypothesis.

Simulations are close to the observations for both the fine- and coarse-resolution simulations (Figure 3). Both scenarios show a general underestimation of $T_w$ under cold/winter conditions. The largest deviations are observed when the water temperature reaches a temperature close to freezing point, at the beginning of the winter. This is likely caused by insufficient buffering in the water bodies, due to an underestimation of the mixing volume present in the lakes and reservoirs during the autumn lake turnover. Other potential causes could be the enhanced ice formation isolating the river channel and the underestimation of runoff and baseflow water temperature which are now related to the air temperature and annual average air temperature, respectively. This behavior is observed for some rivers in the boreal winter, where the model has the tendency to simulate winter water temperatures that are too low compared to the observations.

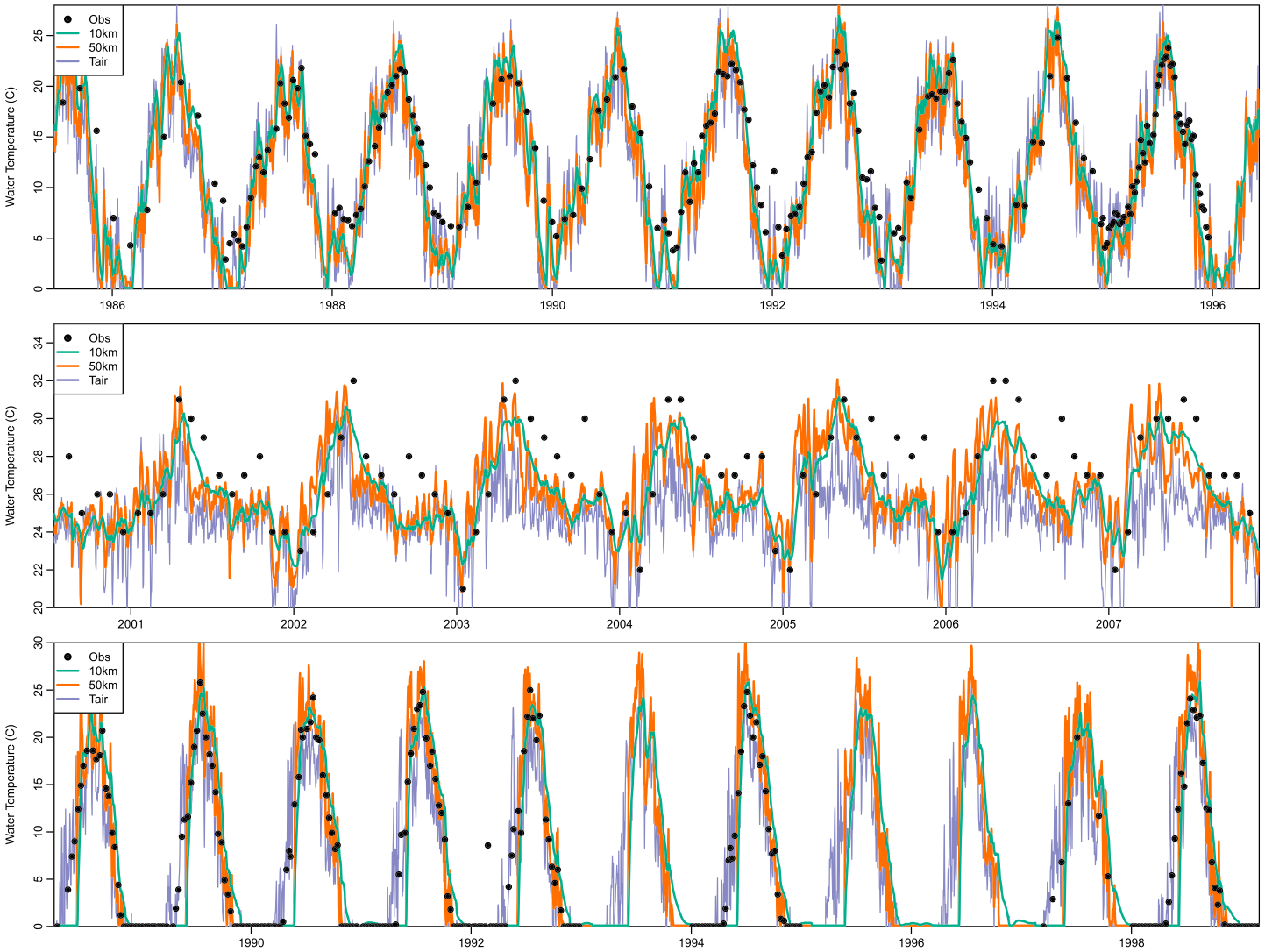


**Figure 3.** Comparison between observations (black dots), high-resolution simulation (green), low-resolution simulation (red), and air temperature model (purple) for the Rhine (top), Mekong (middle), and Tom river (bottom).

Tropical rivers with a lower intra-annual variability tend to be simulated well; the model clearly captures the annual fluctuations that are caused by the seasonal cycle in the discharge and air temperature (Figure 3). Small deviations from the observations are found in winter when the discharge is low. Precipitation events in that time of year cause the river temperature to drop rapidly as a result of the high volume of cold precipitation water on top of the low-channel storage. The extent of this decrease in $T_w$ is underestimated by DynWat, due to the fact that the precipitation temperature is overestimated and assumed to be equal to the air temperature (van Beek et al., 2012). Again, we observe a slower, more smoothed response of the higher-resolution simulations.

Arctic and continental river simulations clearly show the signature freezing-thaw cycle that is also captured by the observational records. For example, in the Tom River in Russia, we see a strong seasonal cycle that is well captured by DynWat in both fine and coarse spatial resolutions. The fine-resolution simulations tend to have a shorter ice cover period, which starts later and often after the observations show frozen conditions. On the other hand, the high-resolution simulations have a better match with the observations for the ice breakup in spring.

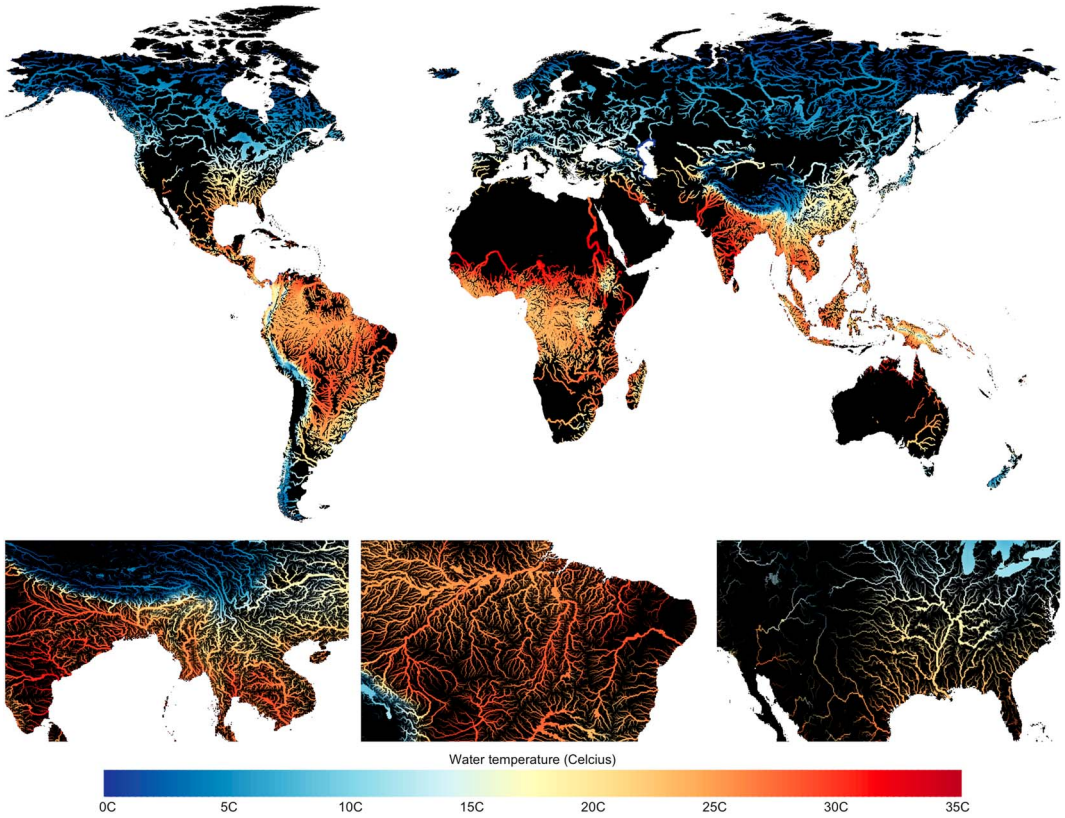


**Figure 4.** Annual average water temperature ($T_w$) for the period 1960–2014; only rivers with more than 10 $m^3/s$ annual average discharge are shown.

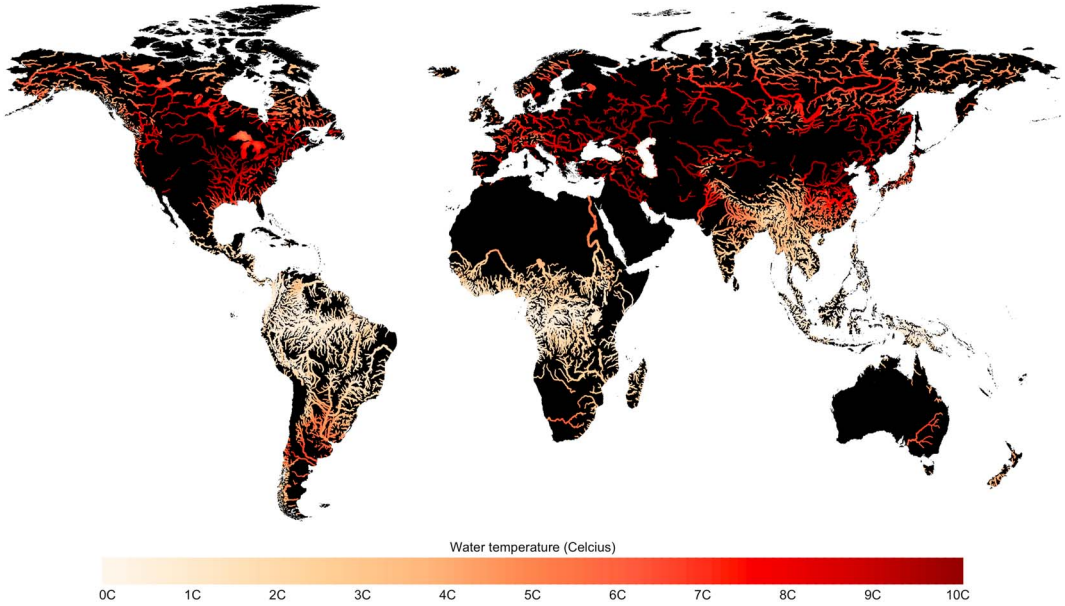


**Figure 5.** Average annual fluctuations in water temperature ($T_w$) for the period 1960–2014; only rivers with more than 10 $m^3/s$ annual average discharge are shown. Fluctuations are computed by calculating the standard deviation of daily $T_w$ values.

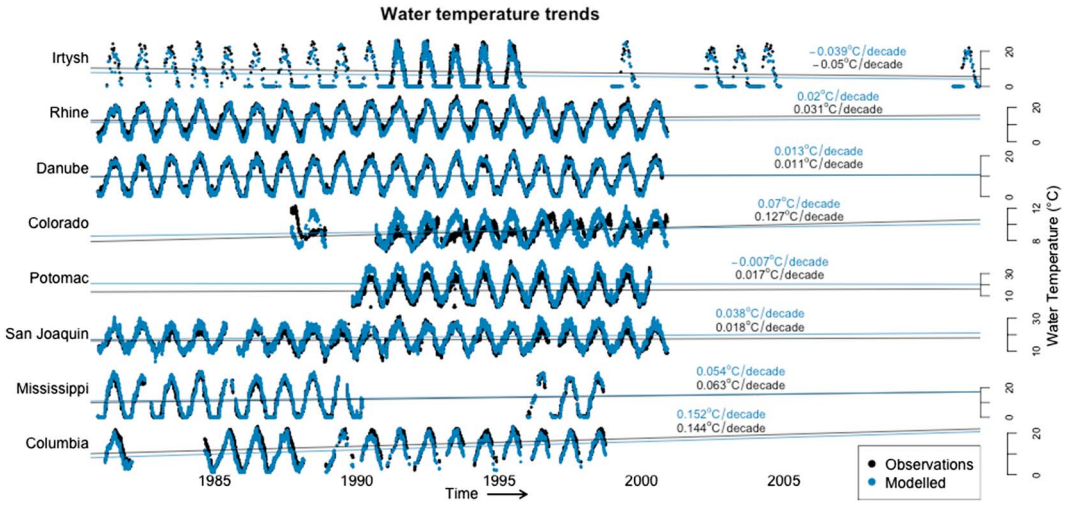


**Figure 6.** Decadal trends in annual mean water temperature ($T_w$) for the period 1960–2014, only rivers with sufficient observations (≥10 years) are shown. Trends are assumed to be linear and the slope coefficients are provided for the observations (black) and high-resolution model simulations (blue).

### 3.2. Spatial Patterns

The spatial patterns of water temperatures clearly show a high correlation with the annual air temperature distribution around the world. Elevated regions in the world's major mountain ranges, the Andes, Alps, Himalayas, and Africa's Eastern Rift mountains, clearly reduce the water temperature compared to the surrounding regions (Figure 4). Regions that experience the largest annual fluctuations in water temperature can be found in the Continental United States and Central Asia, where the continental climate has a big impact on the seasonal cycle of $T_w$ (Figure 5). We see that mountainous regions (e.g., Alps and Himalayas) show relatively stable temperatures caused by the snow and glacier melt, which are the main contributors to the streamflow in these regions. We also find that the tropical regions show a relatively stable temperature regime, due to the relatively constant air temperature and high annual precipitation totals. This leads to large volumes of stored water that have a buffering effect on the fluctuations in the energy influx in the region.

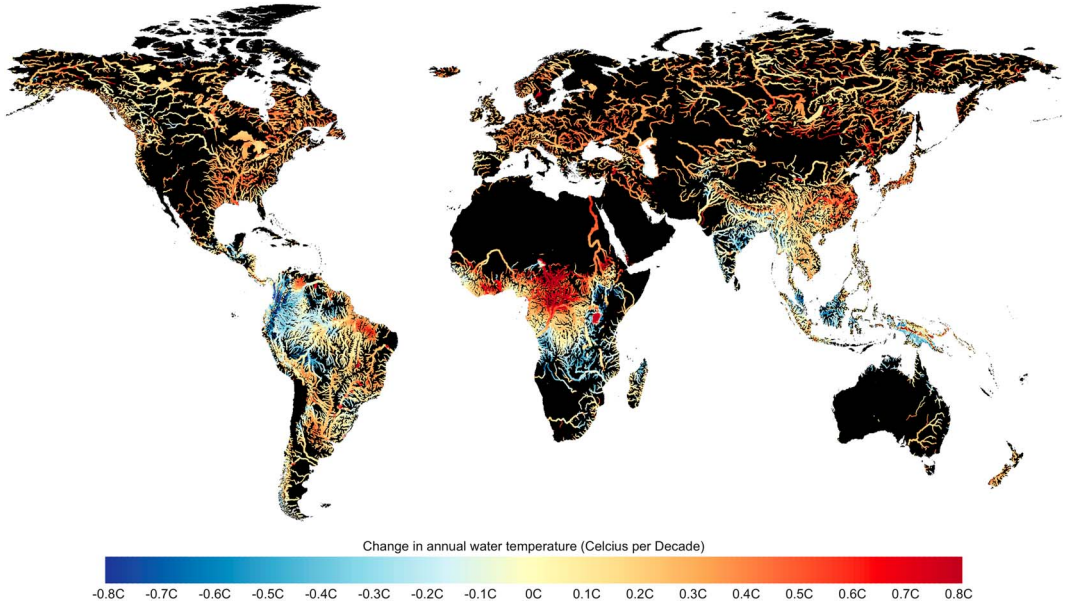


**Figure 7.** Decadal trends in annual mean water temperature ($T_w$) for the period 1960–2014, only rivers with more than 10-$m^3$/s annual average discharge are shown. Trends are assumed to be linear, only significant trends are shown here.

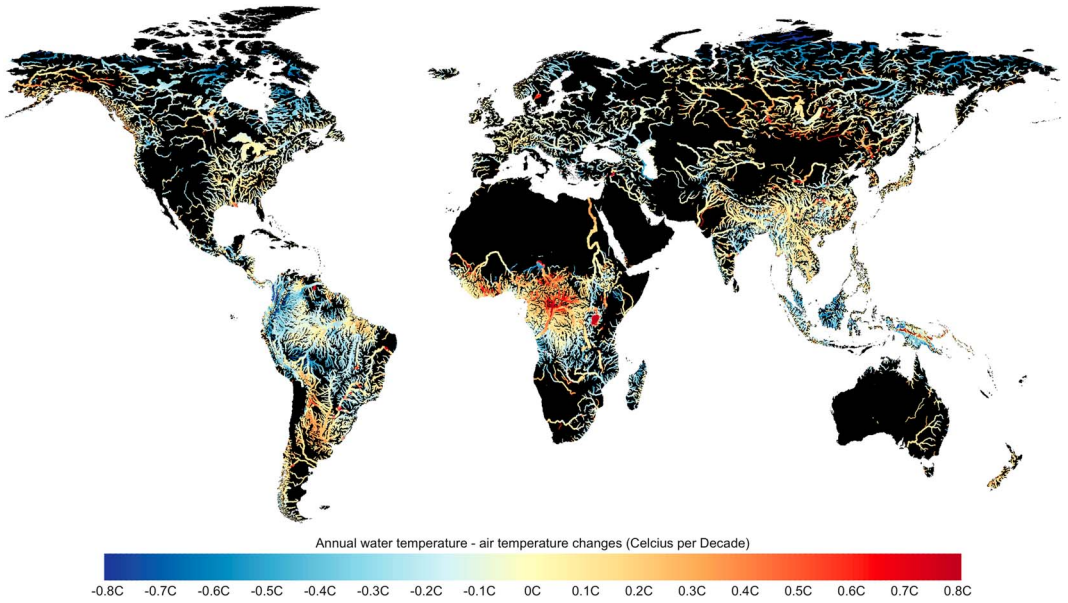


**Figure 8.** Difference in decadal trends in annual mean water temperature ($T_w$) and air temperature ($T_{\text{air}}$) for the period 1960–2014, only rivers with more than 10-$m^3$/s annual average discharge are shown. Trends in $T_w$ and $T_{\text{air}}$ are assumed to be linear, only significant difference between trends are shown here.

### 3.3. Trends

The spatial pattern for the observations is similar to that observed for the simulations (Figure 6). For the limited number of stations with sufficient observational data we find that the simulated and observed trends are in the same order of magnitude and direction. At the global scale, we observe an increase in water temperatures of 0.163 °C per decade, where the Northern Hemisphere clearly shows a strong warming trend (0.22 °C per decade). The tropics show a mixed pattern with distinct regions of water temperature cooling and warming (Figure 7). The strongest increases in the average annual water temperature are found in the Congo river, where we see rivers that have a warming trend close to 1 °C per decade for the period 1960–2014. Some strong decadal increases in water temperature are found in locations where reservoirs were constructed in the period 1960–2014. The reservoir construction resulted in an increased water volume that often results in an increase in the annual average temperature (e.g., Lake Victoria). This is especially true for regions with high air temperature, where the incoming radiation will have a significant warming effect on the reservoir $T_w$. Change in the precipitation pattern can also cause changes in the water temperature. Increased precipitation in summer can lead to increased $T_w$, which will result in a higher annual average $T_w$. This is, for example, the case for Lake Victoria in Africa, where increased precipitation in the warm season (Kizza et al., 2009), in combination with changes in reservoir management, leads to a strong increase in annual $T_w$. For Lake Victoria we observe an increase in annual $T_w$ of 1.0 °C per decade, while the surrounding show limited to no warming. On the other hand, strong cooling in $T_w$ is found in the Amazon region, which is largely consistent with the observed decrease in air temperature in the ERA forcing data and increase of precipitation in the colder winter. The advantage of physically based models becomes evident in these trend analysis, as these models allow to model $T_w$ and streamflow changes in conditions that have previously not been observed (e.g., climate change). They are also capable of mitigating these trends along the river network, to show downstream impacts of the local warming. The Congo shows strong increases in water temperature near the outlet, whereas the rest of the region indicates a cooling in $T_w$.

Further analysis was done by comparing the trends in annual average air temperature with the trends in annual average water temperature (Figure 7). The resulting map (Figure 8) indicates where changes in air temperatures are not the dominant driver for naturalized water temperature changes. We observe that changes in the incoming radiation are an additional driver of water temperature changes, especially in

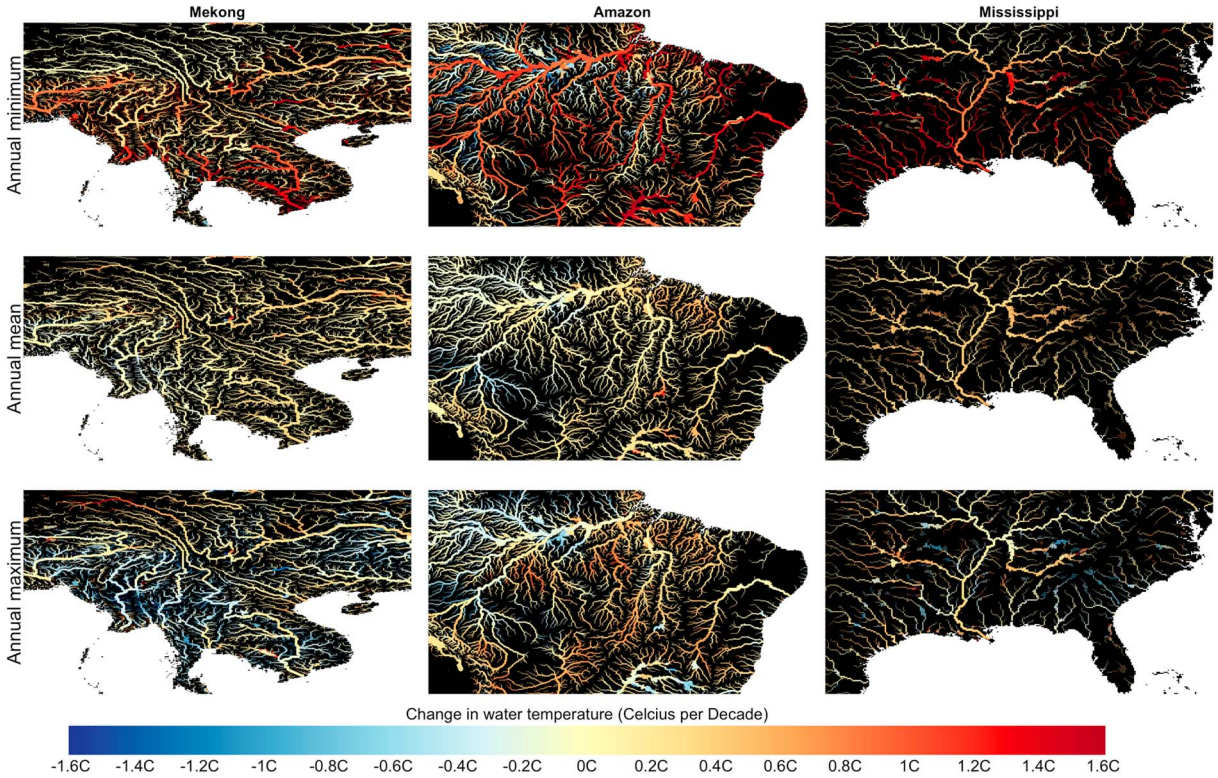


**Figure 9.** Decadal changes in annual minimum (top row), annual mean (middle row), and maximum (bottom row) water temperature.

regions with a reduction in cloud cover (e.g., the Congo river). Strong discrepancies between $T_w$ and $T_{air}$ trends are also found where increased air temperatures lead to a significant increase in the snow and glacier melt. The resulting enhanced cooling effect leads to a strong decrease in annual average water temperatures downstream of the glacier and snow regions (e.g., Himalayas and Andes). Other deviations are found when heat transport to downstream regions causes trend differences between local $T_{air}$ and regional $T_w$ (e.g., Danube, Nile). The differences observed in the Arctic regions of Russia and Canada are attributed to the freezing of rivers, where the annual average $T_w$ is fixed at 0 °C and trends in $T_{air}$ cannot be related to the water temperature. Finally, we note that the inclusion of human-induced local impacts (e.g., cooling water power plants) would likely alter the simulated spatial pattern of temperature difference.

The simulated trends in annual minimum and maximum temperature show a more extreme picture (Figures 9). We see a strong increase in the annual minimum temperature for the Tropics, especially in the major river systems, whereas it is expected that the minimum water temperature in most parts of the high Northern Hemisphere will remain 0 °C.

## 4. Discussion

### 4.1. Evaluation

In general, we observe a very good correspondence between the modeled and observed $T_w$. This indicates that at the locations where we do have observations, DynWat is capable of capturing the temporal dynamics without further need for calibration or discharge estimates from additional data sets. The skill that is observed at these validation sites gives confidence that DynWat (i) can be used at the global scale; (ii) provides accurate $T_w$ estimates and the validation sites; and (iii) can provide reliable input for other applications, like estimating cooling potential for power plants or study the impact of water temperature on biodiversity. It should be noted that it remains difficult to evaluate the performance of DynWat in regions with limited observations like the tropics, but given the general high skill in other regions without calibration it is likely that the model will have a reasonable performance in those regions.

The spatial patterns found in this work show a strong resemblance with the spatial patterns found by earlier studies by van Beek et al. (2012) and other global studies. The spatial pattern is strongly correlated with the spatial distribution of air temperature; however, we observe that strong lateral energy transport occurs in many major river systems in the world. Compared to van Beek et al. (2012) the current model has more water bodies (i.e., reservoirs and lakes) included, which dampen the impact of air temperature changes. We can observe that most of the major river basins show a disconnection between the air temperature trends and the water temperature trends due to the changes in other factors determining water temperature, such as precipitation and evaporation, in combination with the strong lateral energy transport.

### 4.2. Spatial Resolution

The increase in spatial resolution from 50 to 10 km has a positive impact on the model performance in terms of reducing the RMSE and model bias while at the same time increasing the local relevance of the DynWat model. The model shows an increased ability to reproduce stream temperature records at finer spatial resolution, which indicates that the model can be used with confidence at the higher 10-km resolution. Compared to calibrated statistical models (e.g., Laanaya et al., 2017) the physically based uncalibrated models shows a good performance. An advantage of using an uncalibrated physical model is that it theoretically will also allow application in ungauged basins without loss of performance (Hrachowitz et al., 2013). The newly released 10-km resolution water temperature data set will, therefore, help to address the current challenges of providing locally relevant information with uncalibrated globally applicable models (Bierkens et al., 2015; Wood et al., 2011).

The new 10-km simulations will provide additional insight for ecological studies where it is important to have accurate estimates of both flow volumes and water temperatures. For many relevant biochemical processes in the surface water, the key driver of the chemical reactions is the water temperature. We have now provided new insights in the exact temperatures at 10 km spatial resolution. This is especially important in catchments that are smaller than a single 50-km grid cell (91% of the global land area in DynWat). The strong reduction in the simulated temperature biases (Figure 2), indicates that the finer spatial resolution will also help in advancing the global simulation of ecological and chemical processes in smaller catchments.

### 4.3. Model Development

We showed that both the increased spatial resolution and the improved physical realism of the simulations led to improvements in the comparison to observed water temperatures. Although this is encouraging and shows a relatively good match between simulated and observed water temperature, potential areas of improvement can be found in the meteorological forcing data, the hydrological input data, the parameterization of lake and ice processes, more realistic hydrodynamic modeling and finally human impacts on water temperature, such as anthropogenic heat effluents and cold water releases from reservoirs. The meteorological forcing of the model can be improved by changing from the relatively coarse, but globally available, ERA forcing data in combination with statistical elevation downscaling, to a higher quality local or regional data set. Unfortunately, it is difficult to find consistent high-quality forcing data for longer time periods as well as for the global domain. Currently, DynWat uses a precipitation temperature correction of 1.5 °C compared to the actual air temperature; preferably, this correction could be removed and precipitation temperature from either observations or dynamical models could be used as input.

The hydrological input data could be improved by using input from a hydrological model that includes an energy balance and provides temperature estimates of the runoff and baseflow fluxes. PCR-GLOBWB 2 is not able to provide these estimates, but is selected because it provides unique simulations that include the human-water interactions. The parameterization of lakes and ice processes could be improved. Lake mixing processes in DynWat could be improved by including more detailed information on the lake characteristics. Ice process descriptions are currently hampered by the lack of accurate ice formation and breakup process descriptions. The latter is difficult to resolve, while the lake characteristics require more advanced information than currently provided in the GranD database (Lehner et al., 2011). Since DynWat already includes both reservoirs and surface water abstractions, we account for two processes that a significant impact on the water volume and consequently the water temperature in the major water bodies. In the current version of

DynWat the water is transported using a kinematic wave approximation, which cannot resolve back-water effects. This could be important when two river branches with different temperatures join. More realistic routing options exist (e.g., Hoch et al., 2017) but are more computationally expensive and require further development before they can be implemented in DynWat. In the current version of DynWat we assume a constant absorption rate (equation (1)), given the impact of process-like sediment transport and algae growth (which is linked to water temperature), we acknowledge that this is not very likely to occur in real-life situation and a potential point for improving the model. As a solution, satellite imagery could provide better global estimates of the absorption rate for the large river system, or the model could be coupled with algae and sediment transport models. Finally, improvements can be made by including the location of heat effluents (e.g., van Vliet, Wiberg, et al., 2016) and the cold water release from reservoirs. The latter can be included since DynWat already includes reservoirs and their operations.

In conclusion, all of these additions mentioned above are likely to lead to improved water temperature simulations but are currently difficult to achieve due to lack of data. For both human-influenced processes, we also need to make assumptions on the likely operating rules and local regulations. This will make it more difficult to include these additions in DynWat, but even a simple global implementation could already show great potential as demonstrated by van Vliet, Wiberg, et al. (2016) van Vliet, Sheffield, et al. (2016).

### 4.4. Global Patterns

The global patterns of water temperature show a strong correlation with global air temperature patterns, with high temperatures around the equators, and decreasing temperatures with increasing latitudes. The importance of water temperature modeling is evident in the regions with strong seasonal changes in water temperature (e.g., continental climates; USA, Central Asia). The use of a physically based model is also important in regions with a lateral transport of water into adjacent regions with a different temperature regime (Olden & Naiman, 2010). For example, simulations of the Nile show that DynWat water from the southern parts of Egypt and Sudan is transported to the Mediterranean Sea (Figure 8). A physically based approach is required under these circumstances to be able to capture the complex interaction between the atmosphere and the water temperature.

We observe strong trends in the water temperature for the Northern Hemisphere, while cooling trends are observed in large parts of the tropics and southeast Asia. These trends are strongly correlated to the trends in air temperature, but discrepancies are observed in the Arctic regions and the tropics. For larger river systems we observe that the trends in the water temperature can differ substantially from the trends in air temperature, due to the lateral displacement of water. Increasing air temperatures can also lead to increases in snow and glacier melt resulting in an increased contribution of these components to the total runoff (Lutz et al., 2014) and consequently result in a local cooling of the water temperature. As a result statistical models are unlikely to observe these cooling effects due to the complicity of the lateral energy transport (Morrill et al., 2005). This study shows that by including the physically based relationships we can simulate the impact of these changes in the hydrological system on the water temperature.

Finally, we observe clear increasing trends in annual average, minimum and maximum water temperatures. The spatial pattern and associated impact clearly differ across the world and are associated with different processes. Regions with cooling are mainly observed around the equator, where precipitation amounts increase in the cold periods (e.g., Peru, Columbia; March–May). This will reduce the annual average temperature of the precipitation that reaches the river system, resulting in an overall cooling of the river water. Strong patterns in the minimum water temperature are caused by the presence of ice in large regions of the Northern Hemisphere, resulting in a constant annual minimum temperature. This behavior is also observed for the Irtysh (Figure 6), where the annual minima temperature remains 0 °C, resulting in no trend for the annual minimum temperature. The strong increase in the major rivers is the result of increased incoming radiation leading to temperature increases in these larger water bodies with longer travel times. On the other hand, we observe strong trends in the annual maximum temperature for Northern Canada and Russia. The mixed pattern in trends in the annual maximum temperature is a result of the buffering effect of large rivers and lakes, whereas small streams are more prone to air temperature extremes.

The constant increase in water temperatures indicates that future water temperature might show an even stronger response. This was also shown by van Vliet, Yearsley, Ludwig, et al. (2012) van Vliet, van Beek, et al. (2016), and future climate simulation could be extended using the new DynWat model.

## 5. Conclusions

In this work, we have provided the first global 10-km water temperature data set for 1960–2014 and a new Dynamic Water temperature model (DynWat). The new water temperature models include additional processes to cover the breakup of ice, thermal mixing in large water bodies, including a dynamic coupling for surface water abstraction and reservoirs operations to allow for finer spatial resolution simulations. The uncalibrated model shows a good correspondence between the modeled and observed water temperature, providing confidence in the overall quality of the data set in ungauged locations. The newly developed database allows impact modelers and others that require detailed water temperature data to have a readily available data set with high-resolution global coverage. Water temperature is a key driver in chemical and ecological processes and this model and data set could help to better simulate and understand these complex interactions. Potential applications could include the following: computation of cooling water potential; ecological impact assessments; and climate change assessments. Finally, the new publicly available DynWat model also allows new studies to use this stand-alone model and couple it to other hydrological models to produce spatially distributed water temperature simulations for other modeling work.

## Appendix A: Additional Tables and Figures for Clarification

Modelling scenarios are provides in Table A1. The improvements achieved by increased physical modelling realism are provided by Figure A1, where the histograms show the difference between the default and new modelling setup. Finally, the spatial patterns in performance metrics are provided in Figure A2, where most observations are located in Europe and the United States.

**Table A1**
*Different Scenarios Used in This Study*

| Application | Spatial resolution | Spatial downscaling meteorology | Hydrodynamics |
|---|---|---|---|
| 0.0833° | 10 km | Yes | Yes |
| 0.5° | 50 km | No | Yes |
| Tair | 10 km | No | No |

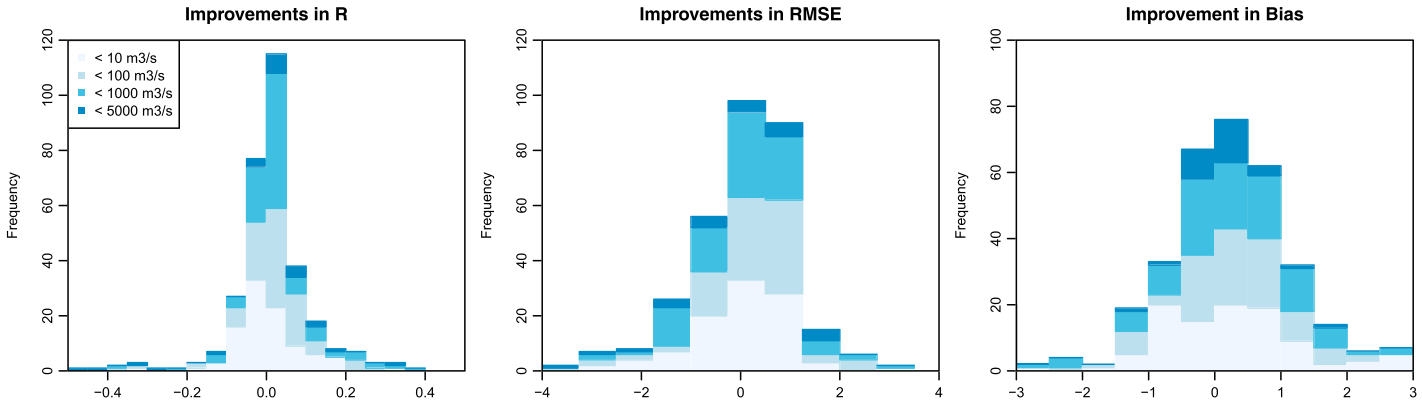


**Figure A1.** Evaluation of improvement in global water temperature simulations at 10 km as a result of including the breakup of ice, thermal mixing in large water bodies, a dynamic coupling for surface water abstraction, and reservoirs operations. Left panel gives the improvements in correlation (R), middle panel the root-mean-square error (RMSE), and right panel provides the bias between observed and simulated water temperatures.

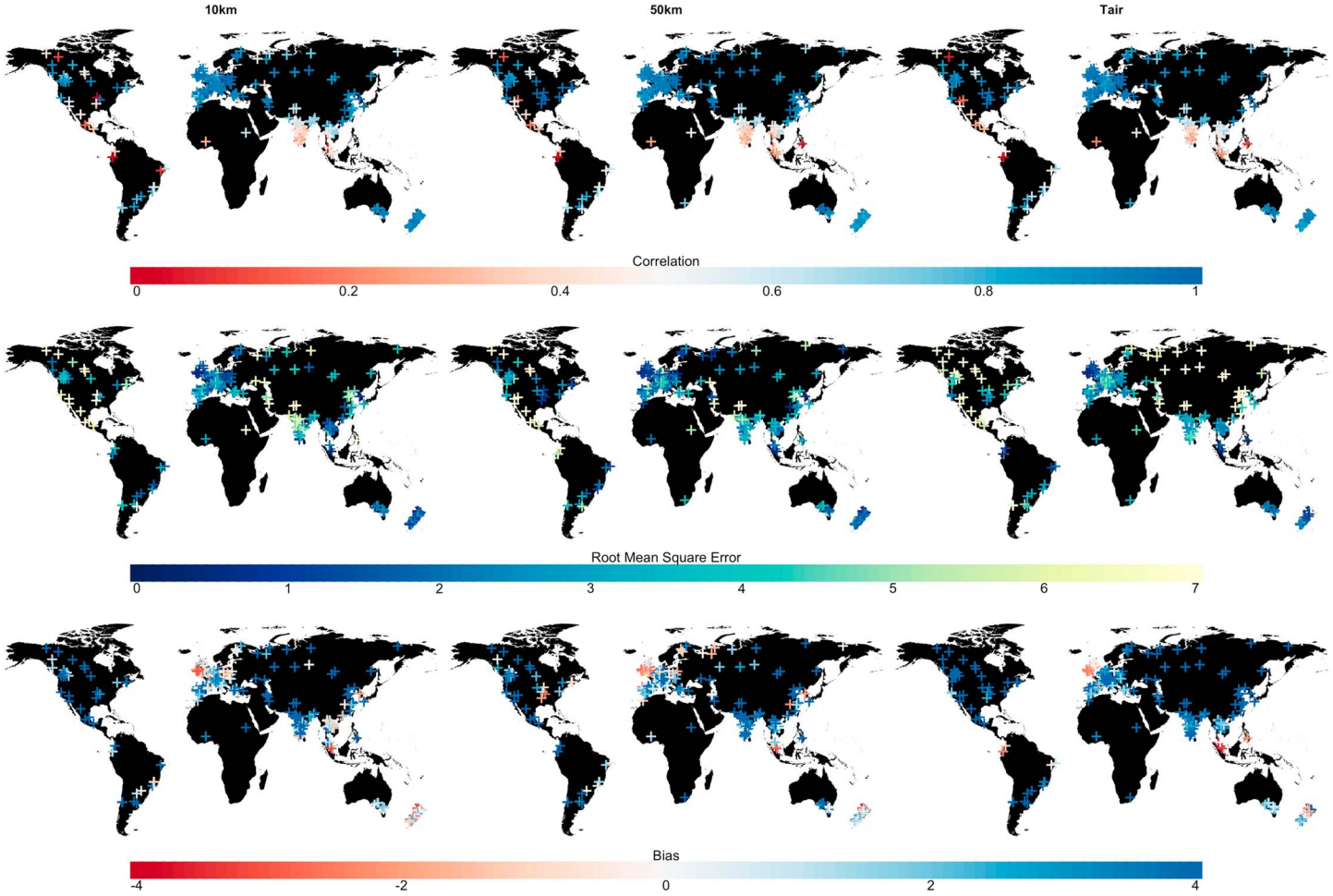


**Figure A2.** Spatial validation of water temperature simulations against observations for correlation (top row), root-mean-square error (middle row), and bias (lower row). Left column gives the high spatial resolution 10-km simulations, middle column is the 50 km, and right column provides the *Tair* comparison model.

**Acknowledgments**
The authors would like to acknowledge the insightful comments provided by the Associate Editor and three anonymous reviewers. N. W. was funded by NWO 016.Veni.181.049. The model code is freely available via this website (https://github.com/wande001/dynWat) and the water temperature data set is available in compressed netCDF4 format via doi:10.5281/zenodo.1468408, at a 10-km spatial resolution. In addition, we provide the spatial discharge simulations in compressed netCDF4 format and 10 km spatial resolution via this website (doi:10.5281/zenodo.1468428).

## References

Berrisford, P., Dee, D. P., Poli, P., Brugge, R., Fielding, K., Fuentes, M., et al. (2011). *The ERA-Interim archive version 2.0* (pp. 23). Reading: Shinfield Park.

Bierkens, M. F. P., Bell, V. A., Burek, P., Chaney, N., Condon, L. E., David, C. H., et al. (2015). Hyper-resolution global hydrological modelling: What is next? *Hydrological Processes*, *29*(2), 310–320.

Bueche, T., & Vetter, M. (2014). Simulating water temperatures and stratification of a pre-alpine lake with a hydrodynamic model: calibration and sensitivity analysis of climatic input parameters. *Hydrological Processes*, *28*(3), 1450–1464.

Byers, H. R., Moses, H., & Harney, P. J. (1949). Measurement of rain temperature. *Journal of Meteorology*, *6*(1), 51–55.

Caissie, D. (2006). The thermal regime of rivers: A review. *Freshwater Biology*, *51*(8), 1389–1406.

Caissie, D., Satish, M. G., & El-Jabi, N. (2007). Predicting water temperatures using a deterministic model: Application on Miramichi River catchments (New Brunswick, Canada). *Journal of Hydrology*, *336*(3-4), 303–315. https://doi.org/10.1016/j.jhydrol.2007.01.008

Davies-Colley, R. J. (1988). Mixing depths in New Zealand lakes. *New Zealand Journal of Marine and Freshwater Research*, *22*(4), 517–528.

DeWeber, J. T., & Wagner, T. (2014). A regional neural network ensemble for predicting mean daily river water temperature. *Journal of Hydrology*, *517*, 187–200.

Dee, D. P., Uppala, S. M., Simmons, A. J., Berrisford, P., Poli, P., Kobayashi, S., et al. (2011). The ERA-Interim reanalysis: Configuration and performance of the data assimilation system. *Quarterly Journal of the Royal Meteorological Society*, *137*(656), 553–597.

Edinger, J. E., Duttweiler, D. W., & Geyer, J. C. (1968). The response of water temperatures to meteorological conditions. *Water Resources Research*, *4*(5), 1137–1143. https://doi.org/10.1029/WR004i005p01137

He, X., Wada, Y., Wanders, N., & Sheffield, J. (2017). Intensification of hydrological drought in California by human water management. *Geophysical Research Letters*, *44*, 1777–1785. https://doi.org/10.1002/2016GL071665

Hoch, J. M., Neal, J. C., Baart, F., van Beek, R., Winsemius, H. C., Bates, P. D., & Bierkens, MarcF. P. (2017). GLOFRIM v1.0—A globally applicable computational framework for integrated hydrological–hydrodynamic modelling. *Geoscientific Model Development*, *10*(10), 3913–3929.

Hrachowitz, M., Savenije, H. H. G., Blöschl, G., McDonnell, J. J., Sivapalan, M., Pomeroy, J. W., et al. (2013). A decade of predictions in ungauged basins (PUB)—a review. *Hydrological Sciences Journal*, *58*(6), 1198–1255.

Kizza, M., Rodhe, A., Xu, C.-Y., Ntale, H. K., & Halldin, S. (2009). Temporal rainfall variability in the Lake Victoria basin in East Africa during the twentieth century. *Theoretical and Applied Climatology*, *98*(1-2), 119–135.

Laanaya, F., St-Hilaire, A., & Gloaguen, E. (2017). Water temperature modelling: Comparison between the generalized additive model, logistic, residuals regression and linear regression models. *Hydrological Sciences Journal*, *62*, 1078–1093.

Lehner, B., Liermann, C. R., Revenga, C., Vörösmarty, C., Fekete, B., Crouzet, P., et al. (2011). High-resolution mapping of the world's reservoirs and dams for sustainable river-flow management. *Frontiers in Ecology and the Environment*, *9*(9), 494–502.

Lessard, J. L., & Hayes, D. B. (2003). Effects of elevated water temperature on fish and macroinvertebrate communities below small dams. *River Research and Applications*, *19*(7), 721–732.

Liebe, J., van de Giesen, N., & Andreini, M. (2005). Estimation of small reservoir storage capacities in a semi-arid environment. *Physics and Chemistry of the Earth, Parts A/B/C*, *30*(6-7), 448–454.

Lutz, A. F., Immerzeel, W. W., Shrestha, A. B., & Bierkens, M. F. P. (2014). Consistent increase in high Asia's runoff due to increasing glacier melt and precipitation. *Nature Climate Change*, *4*(7), 587–592.

Marx, A., Kumar, R., Thober, S., Rakovec, O., Wanders, N., Zink, M., et al. (2018). Climate change alters low flows in Europe under global warming of 1.5, 2, and 3c. *Hydrology and Earth System Sciences*, *22*(2), 1017–1032.

Matthews, K. R., & Berg, N. H. (1997). Rainbow trout responses to water temperature and dissolved oxygen stress in two Southern California stream pools. *Journal of Fish Biology*, *50*(1), 50–67.

Moore, R. D. D. (2006). Stream temperature patterns in British Columbia, Canada, based on routine spot measurements. *Canadian Water Resources Journal*, *31*(1), 41–56.

Morrill, J. C., Bales, R. C., & Conklin, M. H. (2005). Estimating stream temperature from air temperature: Implications for future water quality. *Journal of Environmental Engineering*, *131*(1), 139–146.

Nezhikovskiy, R. A. (1964). *Coefficient of roughness of bottom surface of slush ice cover: Soviet hydrology* (Vol. 2, pp. 127–150). Washington, DC: American Geophysical Union.

Olden, J. D., & Naiman, R. J. (2010). Incorporating thermal regimes into environmental flows assessments: modifying dam operations to restore freshwater ecosystem integrity. *Freshwater Biology*, *55*(1), 86–107.

Ozaki, N., Fukushima, T., Harasawa, H., Kojiri, T., Kawashima, K., & Ono, M. (2003). Statistical analyses on the effects of air temperature fluctuations on river water qualities. *Hydrological Processes*, *17*(14), 2837–2853.

Pike, A., Danner, E., Boughton, D., Melton, F., Nemani, R., Rajagopalan, B., & Lindley, S. (2013). Forecasting river temperatures in real time using a stochastic dynamics approach. *Water Resources Research*, *49*, 5168–5182. https://doi.org/10.1002/wrcr.20389

Punzet, M., Voß, F., Voß, A., Kynast, E., & Bärlund, I. (2012). A global approach to assess the potential impact of climate change on stream water temperatures and related in-stream first-order decay rates. *Journal of Hydrometeorology*, *13*(3), 1052–1065.

Robarts, R. D., & Zohary, T. (1987). Temperature effects on photosynthetic capacity, respiration, and growth rates of bloom-forming cyanobacteria. *New Zealand Journal of Marine and Freshwater Research*, *21*(3), 391–399.

Smith, K. (1981). The prediction of river water temperatures/Prédiction des températures des eaux de rivière. *Hydrological Sciences Bulletin*, *26*(1), 19–32.

St-Hilaire, A., Morin, G., El-Jabi, N., & Caissie, D. (2000). Water temperature modelling in a small forested stream: Implication of forest canopy and soil temperature. *Canadian Journal of Civil Engineering*, *27*(6), 1095–1108. https://doi.org/10.1139/l00-021

Sutanudjaja, E. H., van Beek, R., Wanders, N., Wada, Y., Bosmans, J. H. C., Drost, N., et al. (2018). PCR-GLOBWB 2: A 5 arcmin global hydrological and water resources model. *Geoscientific Model Development*, *11*(6), 2429–2453.

Thober, S., Kumar, R., Wanders, N., Marx, A., Pan, M., Rakovec, O., et al. (2017). Multi-model ensemble projections of European river floods and high flows at 1.5, 2, and 3 degree global warming. *Environmental Research Letters*, *13*, 14003.

Uppala, S. M., Kallberg, P. W., Simmons, A. J., Andrae, U., Bechtold, V. D. C., Fiorino, M., et al. (2005). The ERA-40 re-analysis. *Quarterly Journal of the Royal Meteorological Society*, *131*, 2961–3012.

van Beek, L. P. H., Eikelboom, T., Van Vliet, M. T. H., & Bierkens, M. F. P. (2012). A physically based model of global freshwater surface temperature. *Water Resources Research*, *48*, W09530. https://doi.org/10.1029/2012WR011819

Van Beek, L. P. H., Wada, Y., & Bierkens, M. F. P. (2011). Global monthly water stress: I. Water balance and water availability. *Water Resources Research*, *47*, W07517. https://doi.org/10.1029/2010WR009791

van Vliet, M. T. H., Franssen, W. H. P., Yearsley, J. R., Ludwig, F., Haddeland, I., Lettenmaier, D. P., & Kabat, P. (2013). Global river discharge and water temperature under climate change. *Global Environmental Change*, *23*(2), 450–464.

van Vliet, M. T. H., Ludwig, F., Zwolsman, J. J. G., Weedon, G. P., & Kabat, P. (2011). Global river temperatures and sensitivity to atmospheric warming and changes in river flow. *Water Resources Research*, *47*, W02544. https://doi.org/10.1029/2010WR009198

van Vliet, M. T. H., Sheffield, J., Wiberg, D., & Wood, E. F. (2016). Impacts of recent drought and warm years on water resources and electricity supply worldwide. *Environmental Research Letters*, *11*(12), 124021.

van Vliet, M. T. H., van Beek, L. P. H., Eisner, S., Flörke, M., Wada, Y., & Bierkens, M. F. P. (2016). Multi-model assessment of global hydropower and cooling water discharge potential under climate change. *Global Environmental Change*, *40*, 156–170.

van Vliet, M. T. H., Wiberg, D., Leduc, S., & Riahi, K. (2016). Power-generation system vulnerability and adaptation to changes in climate and water resources. *Nature Climate Change*, *6*(4), 375–380.

van Vliet, M. T. H., Yearsley, J. R., Franssen, W. H. P., Ludwig, F., Haddeland, I., Lettenmaier, D. P., & Kabat, P. (2012). Coupled daily streamflow and water temperature modelling in large river basins. *Hydrology and Earth System Sciences*, *16*(11), 4303–4321.

van Vliet, M. T. H., Yearsley, J. R., Ludwig, F., Vogele, S., Lettenmaier, D. P., & Kabat, P. (2012). Vulnerability of US and European electricity supply to climate change. *Nature Climate Change*, *2*(9), 676–681.

Wada, Y., van Beek, L. P. H., Wanders, N., & Bierkens, M. F. P. (2013). Human water consumption intensifies hydrological drought worldwide. *Environmental Research Letters*, *8*(3), 34036.

Wanders, N., & Van Lanen, H. A. J. (2015). Future discharge drought across climate regions around the world modelled with a synthetic hydrological modelling approach forced by three general circulation models. *Natural Hazards and Earth System Sciences*, *15*(3), 487–504.

Wanders, N., & Wada, Y. (2015a). Human and climate impacts on the 21st century hydrological drought. *Journal of Hydrology*, *526*, 208–220.

Wanders, N., & Wada, Y. (2015b). Decadal predictability of river discharge with climate oscillations over the 20th and early 21st century. *Geophysical Research Letters*, *42*, 10,689–10,695. https://doi.org/10.1002/2015GL066929

Winsemius, H. C., van Beek, L. P. H., Jongman, B., Ward, P. J., & Bouwman, A. (2013). A framework for global river flood risk assessments. *Hydrology and Earth System Sciences*, *17*(5), 1871–1892.

Wood, E. F., Roundy, J. K., Troy, T. J., van Beek, L. P. H., Bierkens, M. F. P., Blyth, E., et al. (2011). Hyperresolution global land surface modeling: Meeting a grand challenge for monitoring Earth's terrestrial water. *Water Resources Research*, *47*, W05301. https://doi.org/10.1029/2010WR010090